Astron. Astrophys. 343, 41–50 (1999)

ASTRONOMY AND ASTROPHYSICS

Microlens diagnostics of accretion disks in active galactic nuclei

A. Yonehara[1,⋆], S. Mineshige[1], J. Fukue[2], M. Umemura[3], and E.L. Turner[4]

[1] Department of Astronomy, Kyoto University, Sakyo-ku, Kyoto 606–8502, Japan
[2] Astronomical Institute, Osaka Kyoiku University, Asahigaoka, Kashiwara, Osaka 582–0026, Japan
[3] Center for Computational Physics, Tsukuba University, Tsukuba, Ibaraki 305–0006, Japan
[4] Princeton University Observatory, Peyton Hall, Princeton, NJ 08544, USA

Received 27 April 1998 / Accepted 20 October 1998

Abstract. The optical-ultraviolet continuum from active galactic nuclei (AGN) seems to originate from optically thick and/or thin disks, and occasionally from associated circumnuclear starburst regions. These different possible origins can, in principle, be distinguished by observations of gravitational microlensing events. We performed numerical simulations of microlensing of an AGN disk by a single lensing star passing in front of the AGN. Calculated spectral variations and light curves show distinct behavior, depending on the nature of the emitting region; time variation over few months with strong wavelength dependence is expected in the case of an optically thick disk (*standard disk*), while an optically thin disk (*advection-dominated disk*) will produce shorter, nearly wavelength-independent variation. In the case of an associated circumnuclear starburst region much slower variations (over a year) will be superposed on the shorter variations caused by microlensing of the disk.

Key words: accretion, accretion disks – galaxies: active – galaxies: nuclei – galaxies: quasars: general – gamma rays: bursts

1. Introduction

There has been long discussion regarding the central structure of active galactic nuclei (AGN). Generally, it is believed that there is a supermassive black hole and a surrounding accretion disk. However, it is quite difficult to obtain direct information about the AGN center, the accretion disk, because the disk size is far too small to resolve. As for cosmological objects, e.g., quasars, the (angular diameter) distance is of the order of $\sim 1\mathrm{Gpc} \sim 3 \times 10^{27}$ cm. If a black hole placed at the center has a mass of $\sim 10^8 M_\odot$, the disk size (say $\sim 1000 r_\mathrm{g}$, where r_g is Schwarzschild radius) will be $\sim 3 \times 10^{16}$ cm. Hence, the apparent disk size (θ_disk) is only $\sim 10^{-11}\mathrm{radian} \sim 1\,\mu$as.

What is usually done is to observe the spectra, which are the sum of local spectra, of the entire disk, and to fit the observed spectra with theoretical integrated spectra. However, there remain ambiguities as to the spatial emissivity distribution. The usual picture is that the so-called UV bump is attributed to blackbody radiation from the standard-type, optically-thick disks (i.e., Shakura & Sunyaev 1973). Such a fundamental model feature may need to be reconsidered due to the recent HST observations that show no big blue bumps (e.g., Zheng et al. 1997).

Instead, microlensing can be used as a 'gravitational telescope' to resolve the disk structure (see Blandford & Hogg 1995; originally proposed by Chang & Refsdal 1984), since a typical Einstein-ring radius of a stellar mass lens is very small; e.g., $\theta_\mathrm{E} \sim 10^{-11}\mathrm{radian} \sim \theta_\mathrm{disk}$ for cosmologically distant sources. With such a gravitational telescope we may be able to obtain information about the disk emergent spectra as a function of distance from the central black hole.

When a point source object is lensed, its luminosity is amplified without any color change. This feature is called 'achromaticity' and is discussed in extensively in the works, following Paczyński (1986; for a review see Narayan & Bartelmann 1996). But, in some actual situations, we cannot treat a source as a point and the effect of a finite source size must be taken into account. Grieger, Kayser, & Refsdal (1988) examined such finite size effects. They simulated microlensing light curves for two different source profiles: stellar-like and accretion disk-like. The light curves show distinct shapes from those of point source calculations. However, they only considered monochromatic intensity variation. Later, Wambsganss & Paczyński (1991) pointed out that if the finite size source has inhomogeneous structure so that each part produces a different spectrum, then the lensing light curves will also have wavelength dependence; i.e., chromatic features in microlensing events will appear. This chromatic effect has been investigated by several authors who calculated microlensing light curves for AGN accretion disk based on simple disk models (e.g., Rauch & Blandford 1991; Jaroszyński, Wambsganss, & Paczyński 1992).

The purpose of this paper is to obtain some criteria for distinguishing disk physics based on more realistic disk models. We adopt the optically-thick, standard-type disk and the more successful, optically thin advection-dominated accretion flow (ADAF; Narayan & Yi 1995; Abramowicz et al. 1995). So far no one (except Yonehara et al. 1998) has calculated X-ray or radio emission in such events, due perhaps to the lack of reliable disk models. However, such calculations are of great impor-

Send offprint requests to: A. Yonehara
⋆ Research Fellow of the Japan Society for the Promotion of Science
Correspondence to: yonehara@kusastro.kyoto-u.ac.jp

tance since X-ray and radio emission seems to originate from the vicinity of the putative black hole. In Sect. 2 we describe our methods of simulation. In Sect. 3 our results are displayed. Sect. 4 is devoted to discussion.

2. Method of the simulation

2.1. Accretion disk models

First, we describe the adopted accretion disk models. We consider two representative types of disks:

2.1.1. Optically thick disk

The first case we consider is the geometrically-thin and optically-thick standard disk (Shakura & Sunyaev 1973). Since we are concerned with disk structure on scales ranging from a few tens to a few thousands of $r_{\rm g}$, we can ignore relativistic effects, such as the gravitational redshift by the black hole. The temperature distribution of the optically thick standard disk is then given by (Shakura & Sunyaev 1973)

$$T(r) = 2.2 \times 10^5 \left(\frac{\dot{M}}{10^{26} {\rm g\ s^{-1}}} \right)^{1/4} \left(\frac{M}{10^8 M_\odot} \right)^{1/4} \times \left(\frac{r}{10^{14}\,{\rm cm}} \right)^{-3/4} \left[1 - \left(\frac{r_{\rm in}}{r} \right)^{1/2} \right]^{1/4} {\rm K}, \quad (1)$$

where $\dot{M}$ is the mass accretion rate and M is the black hole mass. The inner edge of the disk, $r_{\rm in}$, is set to be $r_{\rm in} = 3r_{\rm g}$, the radius of the marginally stable last circular orbit around a non-rotating black hole.

Since the disk is optically thick, we can assume blackbody radiation. Inserting the temperature profile $T(r)$ into

$$\Delta L(\nu, r) = 2 \cdot 4\pi B_\nu \left[T(r) \right] \Delta S \cos\alpha, \quad (2)$$

we can calculate the luminosity of a part of the disk with the surface element, $\Delta S = \Delta r \cdot r \Delta\phi$, at a radius r and a frequency ν, where B_ν is a Planck function (e.g., see Eq. (1.51) of Rybicki & Lightman 1979), and α is the inclination angle of the disk. For simplicity, we assume the disk is face-on ($\alpha = 0$). It might be noted that the radiation spectra do not depend on the viscosity in this standard-type disk, since the total emissivity and the effective temperature are solely determined by the energy balance between the radiative cooling and viscous heating (which originates from release of gravitational energy).

2.1.2. Optically thin disk

The second model is the optically thin version of the advection dominated accretion flow (ADAF). We used the spectrum calculated by Manmoto, Mineshige, & Kusunose (1997) and derive luminosity $\Delta L(\nu, r)$ in the same way as we did for an optically thick disk:

$$\Delta L(\nu, r) = 2 \cdot \epsilon_\nu(r) \Delta S, \quad (3)$$

where ϵ_ν is the surface emissivity which includes the effect of inclination angle (details are given in Manmoto et al. 1997). In this paper, we also set $\alpha = 0$ (face-on) as for the case of optically thick disk. We include synchrotron, bremsstrahlung, and inverse Compton scattering of soft photons created by the former two processes (see Narayan & Yi 1995 for more details). The optical flux is mainly due to Comptonization of synchrotron photons.

In this sort of disk (or flow), radiative cooling is inefficient because of the very low density. As a result, accreting matter falls into a central object, hardly losing any of its internal energy (which is converted from its gravitational energy through the action of viscosity) as radiation. Hence, although the total disk luminosity is less than that of the standard one for the same mass-flow rate, the disk can be significantly hotter, with electron temperatures being of the order of 10^9 K or more, thus producing high energy (X-γ ray) photons. Photon energy is thus widely spread over large frequency ranges. Since emission inside the last circular orbit (at $3r_{\rm g}$) is not totally negligible in this case, we solve the flow structure until the event horizon ($r_{\rm g}$) passing through the transonic point, and consider radiation from the entire region outside the horizon, although the contribution from the innermost part is not dominant. Unlike the optically thick case, the viscosity explicitly affects the emissivity in this case, since radiative cooling depends on density and is no longer balanced with viscous heating (and with gravitational energy release). In the present study, we assign the viscosity parameter to be $\alpha = 0.1$.

2.2. Microlensing events

Although the single lens approximation is not always appropriate to real microlensing events, we consider it here in order to more clearly illustrate the main effects (for extend source effect on microlensing by single lens object, e.g., Bontz 1979).

Generally, the microlensed images are split into two (or more) images. When the separation between these images is too small to resolve, however, the total magnitudes of all the split images vary due to the relative motion of lens and source.

The properties of microlensing have been extensively examined for simple cases where both the lens and source are regarded as being points (e.g., Paczyński 1986). In our simulation, we include the effect of occultation by the lens object, an effect recently pointed out by Bromley (1996). In other words, we consider that the radius of the lens object ($R_{\rm lens}$) is the same as the Sun's, i.e., $R_{\rm lens} = R_\odot = 6.96 \times 10^{10}$ cm. If an image position is smaller than the radius of lens object, we exclude its contribution. Therefore, the total amplification (or magnification) factor A for microlensing is exactly expressed as

$$A(u) = \begin{cases} 0 & \left(\theta_{\rm image,+} < \frac{R_{\rm lens}}{D_{\rm ol}} \right) \\ \frac{u^2+2}{2u(u^2+4)^{1/2}} + \frac{1}{2} & \left(\theta_{\rm image,-} < \frac{R_{\rm lens}}{D_{\rm ol}} \le \theta_{\rm image,+} \right) \\ \frac{u^2+2}{u(u^2+4)^{1/2}} & ({\rm otherwise}), \end{cases} \quad (4)$$

where u corresponds to the angular separation between lens and source in the unit of the Einstein-ring radius and is always greater than or equal to zero, i.e., $u \ge 0$, and $\theta_{\rm image,\pm}$ shows that the image positions of the two microlensed images from a lens object in radians, i.e.,

$$\theta_{\rm image,\pm} = \frac{1}{2}\theta_{\rm E}\left[u \pm \left(u^2+4\right)^{1/2}\right] \tag{5}$$

This function as shown in Eq. 4 as a monotonically increasing function of u; $A(u) \simeq 1.34, \sim 10, \sim 100$ for $u = 1.0, 0.1$, and 0.01.

Here, the Einstein-ring radius is

$$\theta_{\rm E} = \left(\frac{4GM_{\rm lens}}{c^2}\frac{D_{\rm ls}}{D_{\rm os}D_{\rm ol}}\right)^{1/2} \tag{6}$$

where $M_{\rm lens}$ is the mass of a lensing star, c is the speed of light, G is the gravitational constant, and $D_{\rm ls}$, $D_{\rm os}$, and $D_{\rm ol}$ denote the angular diameter distances from lens to source, from observer to source, and from observer to lens, respectively (Paczyński 1986). Adopting an appropriate cosmological model, we can calculate these angular diameter distances in terms of redshifts $z_{\rm ls}$ (from lens to source), $z_{\rm os}$ (from observer to source), and $z_{\rm ol}$ (from observer to lens). In the present study, we assume the Einstein-de Sitter Universe, in which we have

$$D_{\rm x} = \frac{2c}{H_0}\frac{1}{1+z_{\rm x}}\left[1-\frac{1}{(1+z_{\rm x})^{1/2}}\right] \tag{7}$$

(e.g., Padmanabhan 1993), where H_0 is Hubble's constant, and the subscript 'x' stands for 'ls', 'os', or 'ol'.

Since we now consider microlensing effects on an extended source, we must integrate the magnification effects over the entire source plane. We thus, as a next step, need to calculate the angular separation u between a part of the source in question and the lens center (see Fig. 1), from which the amplification factor, $A(u)$, can be found. In the present study, we first divide an accretion disk plane into azimuthal (ϕ) and radial (r) elements. The azimuthal coordinate is equally divided into ~ 1000 segments (ϕ_j), while the logarithmically scaled radial coordinate is also equally divided into ~ 1000 segments (r_i). We then calculate the observed flux at frequency ν from a cell between r_i and r_{i+1} in the radial direction and between ϕ_j and ϕ_{j+1} in the azimuthal direction. Noting that photons emitted by the source at a frequency ν are observed at the frequency $\nu/(1+z_{\rm os})$, we write the observed flux as

$$\Delta F_{\rm obs}(\nu; r_i, \phi_j) \simeq A(u)\Delta F_{\rm obs,0}\left[\nu(1+z_{\rm os}), r_i, \phi_j\right], \tag{8}$$

where $A(u)$ is the amplification factor given by Eq. (4). Moreover, u is explicitly given by

$$u = \left[\left(\frac{r_i}{D_{\rm os}}\cos\phi - \theta_{\rm d}\cos\phi_{\rm lens}\right)^2 + \left(\frac{r_i}{D_{\rm os}}\sin\phi - \theta_{\rm d}\sin\phi_{\rm lens}\cos\alpha\right)^2\right]^{1/2}\theta_{\rm E}^{-1}, \tag{9}$$

where α is the inclination angle of an accretion disk (in this paper, as indicated in Sect. 2.1, we set $\alpha = 0$), and $\theta_{\rm d}$ and $\phi_{\rm lens}$ represent the radial and the azimuthal positions of the lens in units of radians, respectively. A schematic view of the calculated disk is shown in Fig. 1. The intrinsic flux in the absence of a microlensing event, $\Delta F_{\rm obs,0}(\nu, r)$, is calculated from $\Delta L(\nu, r)$ according to

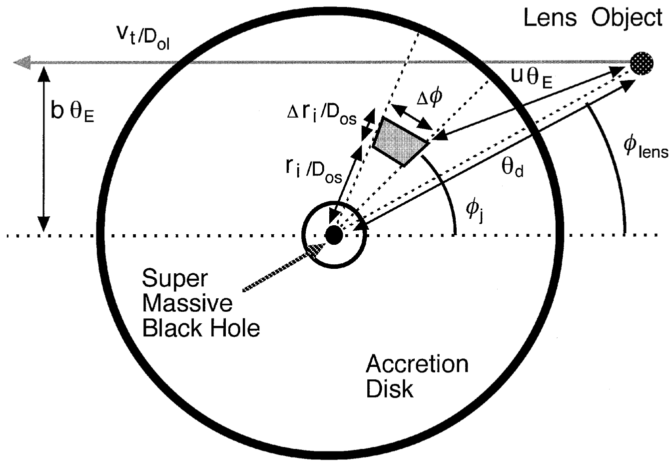

Fig. 1. Schematic view of the calculation of the separation between each cell and lens.

$$\Delta F_{\rm obs,0}(\nu, r) = \frac{\Delta L(\nu, r)}{4\pi D_{\rm os}^2(1+z_{\rm os})^3}, \tag{10}$$

where $\Delta L(\nu, r)$ depends on the disk model (see Eqs. (2) and (3)). In the present study, since we neglected relativistic effects (e.g., beaming, gravitational redshift etc.), $\Delta L(\nu; r, \phi)$ has no azimuthal dependence.

Summing up $\Delta F_{\rm obs}(\nu; r, \phi)$ over the entire disk plane from the inner boundary ($r_{\rm in}$) to the outer boundary ($r_{\rm out}$), we obtain the total observed flux at frequency ν, or the spectrum of the microlensed accretion disk.

3. Results of the calculations

3.1. Model parameters

For clarity, we consider a specific lensed quasar, Q 2237+0305 (the Einstein cross, e.g., Huchra et al. 1985). Irwin et al. (1989) reported an increase of the apparent luminosity of image A by ~ 0.5mag on a timescale of a few months, which was nicely reproduced by a model of microlensing (Wambsganss, Paczyński, & Schneider 1990). At present, at least five microlens events have been reported so far in the Q2237+0305 images (Irwin et al. 1989; Corrigan et al. 1991; Houde & Racine 1994). Although the single lens treatment for Q 2237+0305 may be a poor approximation (see discussion), we just take this object as one test case and derive quite general conclusions regarding the generic observational features of microlensed accretion disks.

This object is macrolensed by a foreground galaxy, and the source is split into four (or five) images. Now, we suppose that one of the macrolensed image is further microlensed by a star in the foreground galaxy causing the macrolensing. Although the macrolensed images are actually affected by two effects, so called, 'convergence' and 'shear', we here neglect both for simplicity and thus assume that the macrolensed image is neither amplified nor distorted. The redshift parameters are

$$z_{\rm os} = 1.675,\ z_{\rm ol} = 0.039 \tag{11}$$

(cf. Irwin et al. 1989), and substitute them into the relation

$$1 + z_{\rm ls} = \frac{1 + z_{\rm os}}{1 + z_{\rm ol}} \tag{12}$$

which can be obtained from flux conservation of radiation (e.g., Padmanabhan 1993), we get

$$z_{\rm ls} = 1.575. \tag{13}$$

As for Hubble's constant, we adopt the value obtained by Kundić et al.(1997), $H_0 \sim 60\,{\rm km\,s^{-1}Mpc^{-1}}$. The adopted disk parameters are the outer edge of the disk, $r_{\rm out} = 10^3 r_{\rm g}$, the mass of the central black hole, $M = 10^8 M_\odot$, and the mass-flow rates, $\dot{M} = 10^{26}\,{\rm g\,s^{-1}}$ for the standard disk and $\dot{M} = 10^{22}\,{\rm g\,s^{-1}}$ for the optically thin disk. We take different mass-flow rates for two cases for computational convenience. This is not, fortunately, a serious problem, since it has been demonstrated that the spectral shape of the ADAF is not very sensitive to $\dot{M}$, although the overall flux level does change. We will not consider the absolute flux in the following discussion, and focus instead on the relative spectral shape and relative flux variation. For other basic parameters characterizing the disks, see Sect. 2.1.

For simplicity, we assume that the accretion disk is face-on; i.e. $i = 0$, to the observer. Actually, based upon a grand unified paradigm of AGNs, quasars are not far from face-on views. We also assume the mass of a lensing object to be $M_{\rm lens} = 1.0 M_\odot$ or $0.1 M_\odot$. The remaining variable is the angular separation (u) between the lens and a part of the source in question.

Adopting these parameters, apparent angular accretion disk size ($\theta_{\rm disk}$) and Einstein ring radius ($\theta_{\rm E}$) is $\theta_{\rm disk} \sim 6.8 \times 10^{-12}{\rm rad}$ and $\theta_{\rm E} \sim 3.3 \times 10^{-11}{\rm rad}$. These values are comparable and we can use such a microlensing event as an effective 'gravitational telescope' (Blandford & Hogg 1995).

3.2. Spectral variation

First, we calculated the microlensed spectra of each of two types of accretion disks for the angular separation between the lens and the source of $u = 1.0$, 0.1, and 0.01, respectively. The results are shown in Fig. 2 for the standard disk (in the upper panel) and for the optically thin disk (in the lower panel), respectively. For the former disk not only the disk brightening, but also substantial spectral deformation is produced by microlensing, when the angular separation is small (Rauch & Blandford 1991; Jaroszyński, Wambsganss, & Paczyński 1992). The smaller the angular separation is, the larger the modification of the observed spectrum. In other words, the amplification factor depends on the frequency (wavelength) of the emitted photons. This gives rise to frequency-dependent, microlensing light curves (see Sect. 3.3). As for the optically thin disk, in contrast, there will not be large spectral modification by microlensing, but the flux is amplified over wide frequency ranges.

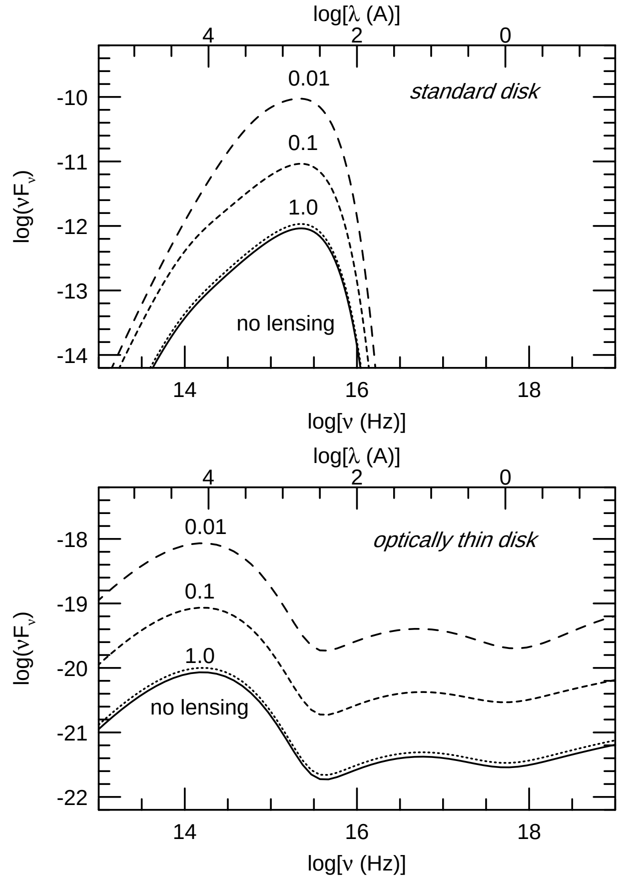

Fig. 2. Microlensed spectrum of a standard accretion disk (*upper*) and an optically thin accretion flow (*lower*). In each panel, the microlensed spectra are plotted for angular separations between the disk center and the lensing star as $u = 1.0$ (dotted line), 0.1 (dashed line), and 0.01 (long dashed line), together with the one in the absence of microlensing (solid line). The lensing mass is $M_{\rm lens} = 1.0 M_\odot$.

To understand such spectral properties, we divide the disk plane into three parts; $r \leq 10 r_{\rm g}$, $10 r_{\rm g} < r < 100 r_{\rm g}$, and $10^2 r_{\rm g} < r < 10^3 r_{\rm g}$, and plot the spectrum from each part of the disk, together with the integrated spectra, in Fig. 3.

In the case of the optically thick accretion disk, photons emitted from different radii have different dominant frequencies because the local temperature of the disk has a strong radial dependence, $T \propto r^{-3/4}$ (Eq. [1]). Note that without lensing the total spectrum has a peak at $\nu \sim 10^{15.3}$ Hz, but its low-frequency part has a smaller slope ($\nu F_\nu \propto \nu^{4/3}$) than that of blackbody radiation ($\nu F_\nu \propto \nu^3$), thus a shoulder like feature extending to $\nu \sim 10^{14}$ Hz ($\sim 30000\,$Å) is formed. This is because the outer cooler portions also contribute to the spectrum. For $u = 0.01$, therefore, the emission only from the inner, hottest part is strongly magnified. This greatly increases a peak at $\nu \sim 10^{15.3}$ Hz ($\sim 1500\,$Å), but a shoulder like feature at $\nu \sim 10^{14}$ Hz ($\sim 30000\,$Å) is weakened.

To further clarify the situation, we also plot the radial distribution of emitted photons at several wavelengths in Fig. 4. The upper panel of Fig. 4 shows a rather gradual change of each flux over a wide spatial range. This reflects the fact that viscous

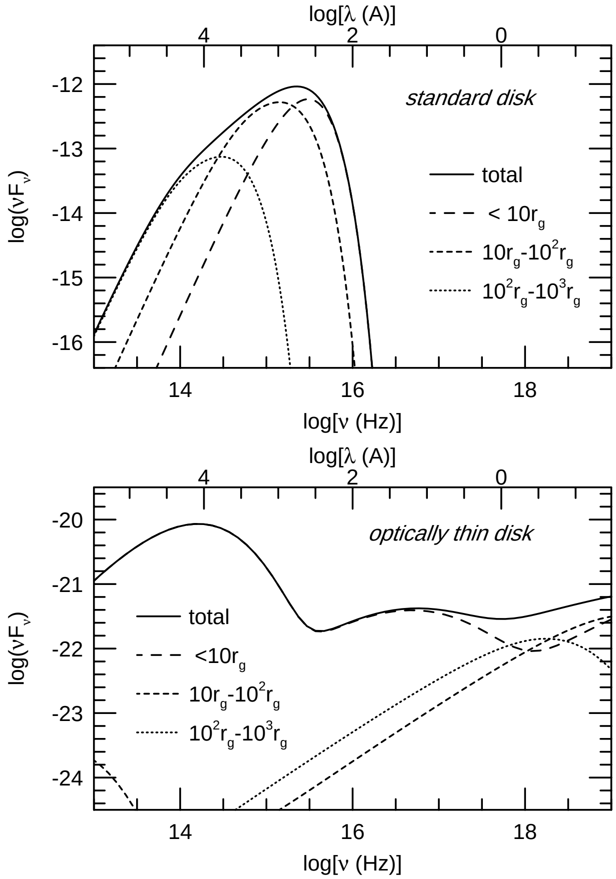

Fig. 3. Contribution to the total integrated spectra from different parts of disks for the cases of a standard (*upper*) and optically thin (*lower*) disk, respectively. Each figure displays the contributions from the inner region of $r \le 10r_{\rm g}$ (long dashed line), the intermediate region of $10r_{\rm g} \sim 100r_{\rm g}$ (dashed line), and the outer region of $10^2r_{\rm g} \sim 10^3r_{\rm g}$ (dotted line).

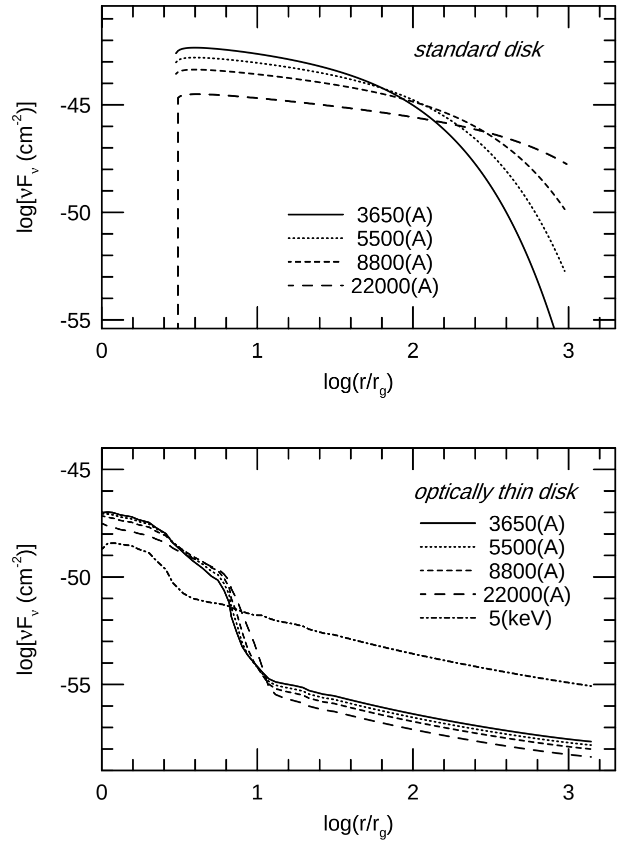

Fig. 4. The radial distribution of the emergent flux at several wavelengths for the case of a standard-type disk (*upper*) and an optically thin disk (*lower*), respectively. The adopted bands are U-band (3650 Å, by the solid line), V-band (5500 Å, by the dotted line), I-band (8800 Å, by dashed line), K-band (22000 Å, by long dashed line), and X-ray (5 keV, by the dot-dashed line).

heating and radiative cooling are balanced in the standard disk. Since the potential energy only gradually changes with the radius, so does the viscous heating rate and the radiative cooling rate. Moreover, the lower a photon frequency is, the wider the parts of the disk in which it is generated.

In the optically-thin accretion disk, on the other hand, the optical-UV flux is totally dominated by that from the inner region ($r \le 10r_{\rm g}$). The lower panel of Fig. 4 clearly shows that almost 100% of optical flux originates from the region inside $10r_{\rm g}$, and that the contribution from the outer parts is smaller by several orders. This is possible in an ADAF, since radiative cooling is no longer directly related to the shape of the gravitational potential well (which has a rather smooth profile). The reason why optical flux is produced in a rather restricted region inside $10r_{\rm g}$ is due to enhanced synchrotron emission in the vicinity of the black hole, where density and pressure (and thus magnetic pressure) are likely to be at maximum within the flow. Nearly irrespective of the u value, as a consequence, it is always the innermost region (within 10 $r_{\rm g}$) that dominates the entire disk spectrum. The amplification of the total emission just reflects that of the emission from the innermost parts. Therefore, the overall flux will be amplified by lensing without large spectral changes.

Fig. 4 also shows that X-rays are produced over a wider range; the contribution from the outer part at 100–$1000r_{\rm g}$ is not negligible at a frequency of $\nu \sim 10^{18}$ Hz (a few keV). This is because of a bremsstrahlung emission from high-temperature electrons (with $T_{\rm e} \sim 10^9\ K$ being maintained at $r \lesssim 100r_{\rm g}$, see Manmoto et al. 1997). We can thus predict that small frequency dependence will be seen in X-rays in this model.

3.3. Light curves

Using the results of the previous subsection, we now calculate light curves during the microlensing events (see Fig. 1). We continuously change the angular separation between the lens and the center of the accretion disk ($\theta_{\rm d}$) according to

$$\theta_{\rm d} = \theta_{\rm d}(t) = \theta_{\rm E}\left[b^2 + \left(\frac{v_{\rm t}t}{D_{\rm ol}\theta_{\rm E}}\right)^2\right]^{1/2}, \qquad (14)$$

and calculate the flux at each frequency, where b is the impact parameter (in the unit of $\theta_{\rm E}$), $v_{\rm t}$ is the transverse velocity of the lens and t is the time. Note that $v_{\rm t}$ also includes the transverse

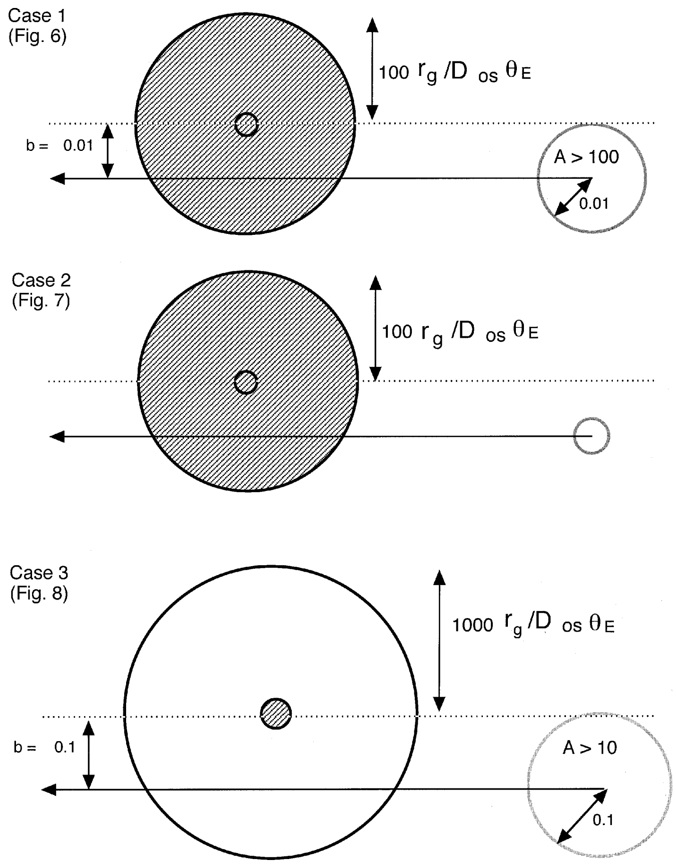

Fig. 5. A schematic view of the microlensing events which we have calculated. These figures show the relative sizes of the accretion disk, impact parameter, and the Einstein-ring radius. In each panel, the shaded regions correspond to a disk with a radius of $100r_{\rm g}$. The *top panel* (Case 1) shows a microlensing event with $(b, M_{\rm lens}) = (0.01, 1.0M_{\odot})$. On the left, the thick outer and inner circles correspond to the radii of $100r_{\rm g}$ and $10r_{\rm g}$, respectively. The right circle corresponds to $\sim 0.01\theta_{\rm E}$. Inside this circle, the amplification factor caused by microlensing is more than 100. The *middle panel* (Case 2) shows a microlensing event with $(b, M_{\rm lens}) = [0.01(M_{\odot}/M_{\rm lens})^{1/2}, 0.1M_{\odot})]$. The circles at the left are the same as those in the *top panel*. The *bottom panel* (Case 3) shows a microlensing event with $(b, M_{\rm lens}) = (0.1, 1.0M_{\odot})$. on the left, the thick outer and inner circles correspond to $1000r_{\rm g}$ and $100r_{\rm g}$ of the accretion disk. The right circle corresponds to $\sim 0.1\theta_{\rm E}$, where the amplification factor caused by microlensing is more than ~ 10.

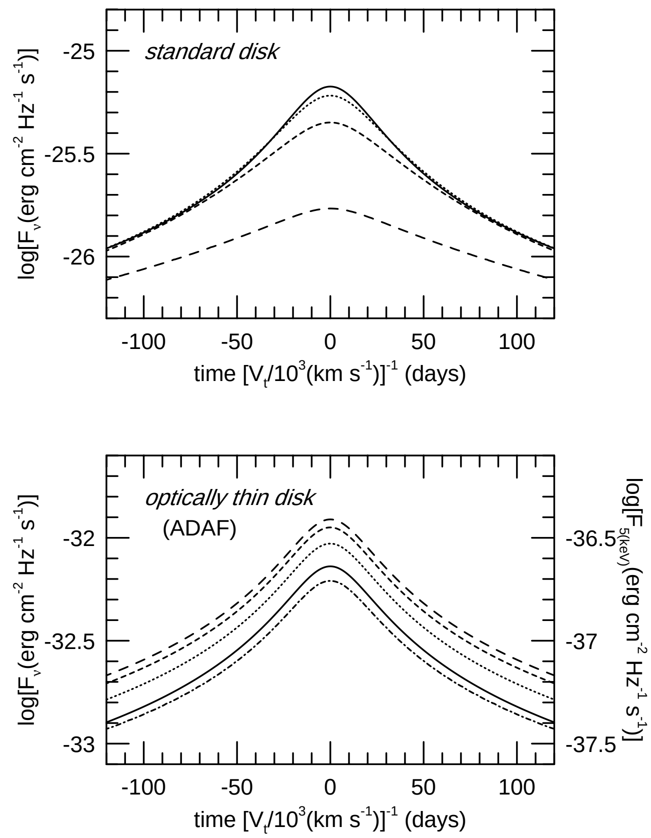

Fig. 6. The microlensed light curves of the standard disk (*upper*) and of the optically thin flow (*lower*). The parameters are $(b, M_{\rm lens}) = (0.01, 1.0M_{\odot})$ (Case 1). The different types of lines correspond to those in Fig. 4.

velocity due to the peculiar motion of the foreground galaxy relative to the source and the observer. We calculated three cases (see Fig. 5).

Fig. 6 shows the microlensing light curves of optically thick (upper panel) and thin (lower panel) disks for the case with $(b, M_{\rm lens}) = (0.01, 1.0M_{\odot})$ (Case 1). The light curve of the optically thin disk is achromatic due to its flat temperature distribution, whereas the light curve of the optically thick one shows strong frequency dependence.

Fig. 4 is useful to understand this chromaticity and achromaticity. Since the spatial flux distribution is similar for different optical fluxes in the case of optically thin disks, each optical flux is amplified in a similar way and thus the color does not change. The x-ray emitting region is wider than that of optical flux, so a small chromaticity may appear when we compare optical and X-ray variations.

In an optically thick disk, conversely, the low-energy photons are created over a wider spatial range, compared to the high-energy photons. If a microlensing event occurs, therefore, the low-energy emission will be the first to be amplified, followed by significant amplification of high-energy emission. Note that each optical flux has the same level at the beginning (at -120 day) in the upper panel of Fig. 6, whereas higher-energy optical flux is greater than that of lower-energy flux in the intrinsic spectra in the absence of lensing (see Fig. 3). This indicates that the amplification of lower-energy flux is already appreciable at $t = -120$ day. This produces the color change.

3.4. Parameter dependence

Fig. 7 shows the light curves for the case with a smaller lensing mass by one order-of-magnitude and the same physical impact parameter ($b\theta_{\rm E}$) (Case 2). Namely, $(b, M_{\rm lens}) = [0.01(M_{\odot}/M_{\rm lens})^{1/2}, 0.1M_{\odot}]$. We see that if the lens mass is small, the peak magnification is reduced but the variability timescale is nearly the same, while the chromaticity of the stan-

Table 1. The calculated fluxes at 3650 Å (*U*-band) and 22000 Å (*K*-band) at different epochs for cases 1,2, and 3. The second and third columns indicate the adopted accretion disk models and the energy band. The fourth, fifth, and sixth columns show the observed fluxes at $t = 200$ d (or -200 d), 100 d (or -100 d), and 0 d. The seventh and eighth columns display changes in the fluxes from $t = -200$ d to $t = -100$ d, and those from $t = -100$ d to $t = 0$ d, respectively.

Case	disk model	band	$\log F_{(200\mathrm{d})}$	$\log F_{(100\mathrm{d})}$	$\log F_{(0\mathrm{d})}$	$\log[F_{(100\mathrm{d})}/F_{(200\mathrm{d})}]$	$\log[F_{(0\mathrm{d})}/F_{(100\mathrm{d})}]$
Case 1	standard	U	−26.179	−25.883	−25.174	0.296	0.709
		K	−26.288	−26.061	−25.766	0.227	0.305
	ADAF	U	−33.113	−32.820	−32.139	0.293	0.681
		K	−32.885	−32.592	−31.910	0.293	0.682
Case 2	standard	U	−26.667	−26.380	−25.674	0.287	0.706
		K	−26.775	−26.555	−26.264	0.220	0.291
	ADAF	U	−33.600	−33.317	−32.638	0.283	0.679
		K	−33.372	−33.089	−32.410	0.283	0.679
Case 3	standard	U	−26.340	−26.247	−26.203	0.093	0.044
		K	−26.446	−26.352	−26.311	0.094	0.041
	ADAF	U	−33.273	−33.180	−33.137	0.093	0.043
		K	−33.045	−32.952	−32.909	0.093	0.043

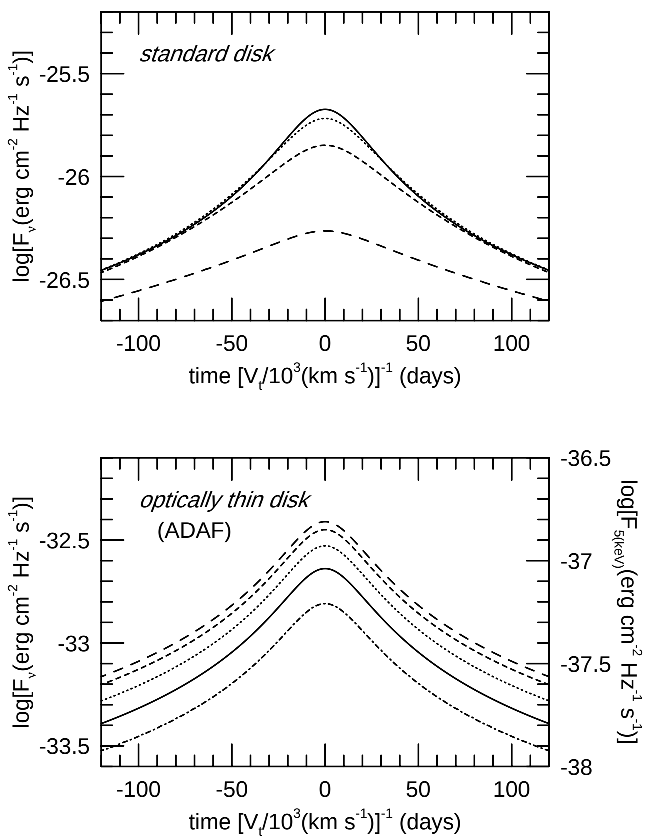

Fig. 7. Corresponds to Fig. 6 but for the case with a smaller lensing mass; $(b, M_{\mathrm{lens}}) = [0.01(M_\odot/M_{\mathrm{lens}})^{1/2}, 0.1M_\odot)]$ (Case 2).

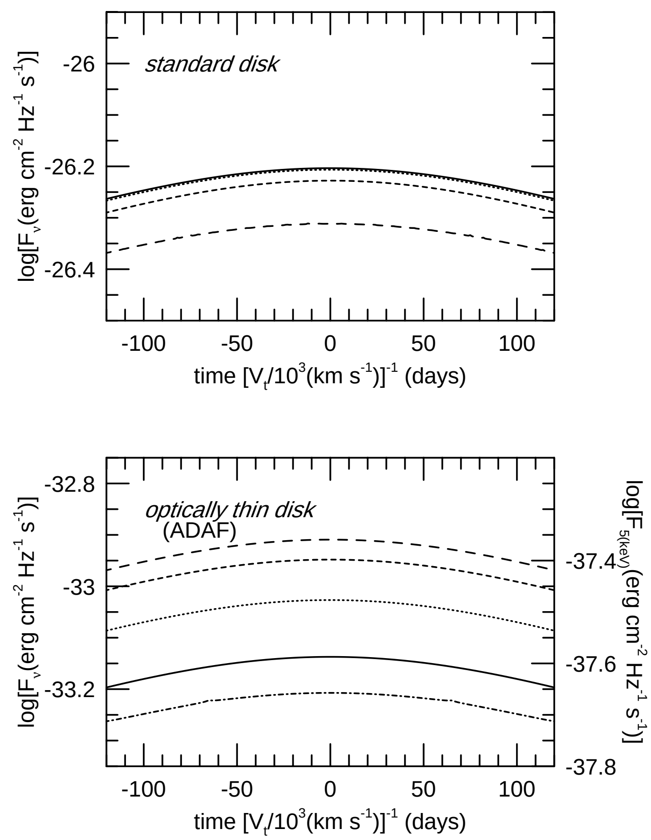

Fig. 8. Corresponds to Fig. 6 but for the case with a larger impact parameter; $(b, M_{\mathrm{lens}}) = (0.1, 1.0M_\odot)$ (Case 3).

dard disk event is still expected. This is more clearly shown in Table 1.

Next, in Fig. 8, we assign a larger impact parameter; $(b, M_{\mathrm{lens}}) = (0.1, 1.0M_\odot)$ (Case 3). In this case, the total amplification and the chromaticity of standard disks models are sharply reduced. Consequently, when we try to distinguish disk structure, our success will depend not so much on the lens mass, but on whether the impact parameter is small or not. We will discuss this issue later (in Sect. 4).

In Table 1, we summarize characteristic values of these three light curves. Achromatic and chromatic features are clear in this table.

Finally, Fig. 9 shows the dependence of the spectrum on the lens mass. The smaller the lens mass is, the narrower the

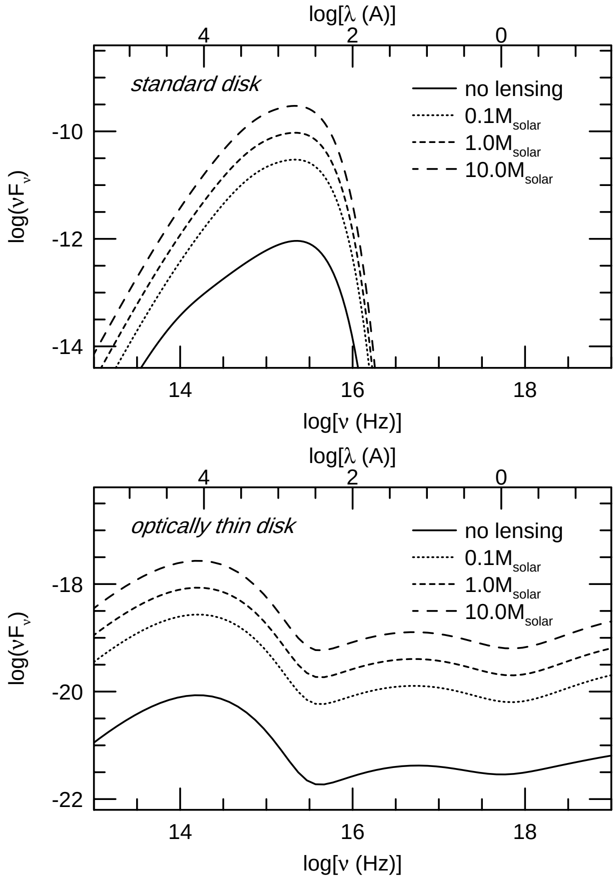

Fig. 9. The dependence of the microlensed spectra of the standard disk (*upper*) and the optically thin flow (*lower*) on the lensing mass, $M_{\rm lens} = 0.1M_\odot$ (dotted line), $1.0M_\odot$ (dashed line), and $10.0M_\odot$ (long dashed line). The impact parameters are $0.01(M_\odot/M_{\rm lens})^{1/2}$. The spectrum without microlensing is also plotted as a solid line.

resulting spectrum above a given flux value becomes. This is because when the lens mass is small, the Einstein-ring radius is small ($\theta_{\rm E} \propto M_{\rm lens}^{1/2}$, see Eq. [5]), and so is the size of the region undergoing microlensing amplification. This naturally reduces the total light amplification.

4. Discussion

We have demonstrated how spectral behavior and microlensing light curves depend on the disk structure. We considered two representative disk models: the standard-type disk emitting predominantly optical-UV photons, and the optically thin, advection-dominated flow (ADAF) producing a wide range of photons from radio to X-γ rays. Using microlensing events light curves, we can hope to distinguish the different possible emissivity distributions of AGN accretion disks and may be able to map them in detail.

At the peak of a microlensing event, when the inner part of the accretion disk is highly amplified, the distinctions between the two disk models are most evident (especially if the impact parameter is small). Thus, only broad band photometry will be required to detect the color changes as shown in Fig. 6, thereby revealing the structure of AGN accretion disks.

Fortunately, such observations do not require good time resolution; for example, once per night, similar to that used for the MACHO project (e.g., Alcock et al. 1998), is sufficient. A typical timescale for a microlensing event is characterized by the Einstein ring crossing time of a lens object expressed as by

$$\frac{\theta_{\rm E}}{v_{\rm t}/D_{\rm ol}} \simeq 6 \times 10^6 \left(\frac{M_{\rm lens}}{M_\odot}\right)^{1/2} \times \left(\frac{v_{\rm t}}{200\,{\rm km\,s^{-1}}}\right)^{-1} \left(\frac{\tilde{D}}{10{\rm kpc}}\right)^{1/2} {\rm s}, \quad (15)$$

where $\tilde{D}$ means $D_{\rm ls}D_{\rm ol}/D_{\rm os}$. For MACHO-like events, when all the factors in the parentheses of Eq. (15) are of order unity, the event timescales become $\sim 0.2\,$yr. For the cosmological quasar case, on the other hand, we find roughly $\tilde{D} \sim 1{\rm Gpc} = 10^5 \times 10{\rm kpc}$, and thus, the third parenthesis is larger by factor ~ 300, yielding event timescales up to $\sim 60\,$yr. Thus, in principle, a few years of observations are sufficient to obtain some information about the central disk structure. Practically, reconstruction of disk structure from a microlensing light curve, that is the so-called 'inverse problem', is not so easy, and will probably require well sampled and high accuracy light curves to overcome the inherent instability of such calculations (e.g., Grieger, Kayser, & Schramm 1991).

To summarize the distinct properties of the two types of disks, we plot in Fig. 10 the differences in the amplification factors at two different frequencies. As the angular separation between the lens and the disk center (u) decreases, ΔF increases (thus the points move in the upper right direction in Fig. 10). Obviously, the color changes are more pronounced in the right panel (between the U- and K-bands) than in the left panel (between the U- and V-bands), and for smaller impact parameters. We can easily distinguish disk structure by comparing the optical and IR fluxes if $b \lesssim 0.03$. Furthermore, as clearly seen in Fig. 10, the wider the separation between the two observed wavelengths are, the more apparent the differences between the light curves of the two disk models become. Owing to this fact, the widely spaced bands are preferable for disk mapping.

As a first step toward understanding the microlensing disk diagnostic, we have considered microlensing by a single star in the present study. However, microlensing events caused by a single lens, especially for cases in which the differences between the light curves of the two disk models are apparent (i.e., $b \leq 0.1$), will not be frequent for actual objects. We thus need to evaluate the average time interval $\langle\Delta t\rangle$ between microlensing events with an impact parameter smaller than b. From Paczyński (1986), we find that $\langle\Delta t\rangle$ is proportional to b^{-1}. If we define events by an impact parameter $b \leq 1.0$, one microlensing event in which we are interested will occur among 10 $(b = 0.1)$ to 100 $(b = 0.01)$ total events.

For example, we here assume parameters for the case of Q 2237+0305, although a single-lens assumption is probably invalid for this object because of its relatively large optical depth for microlensing (e.g., $\tau = 0.4 \sim 0.7$ from Rix, Schneider,

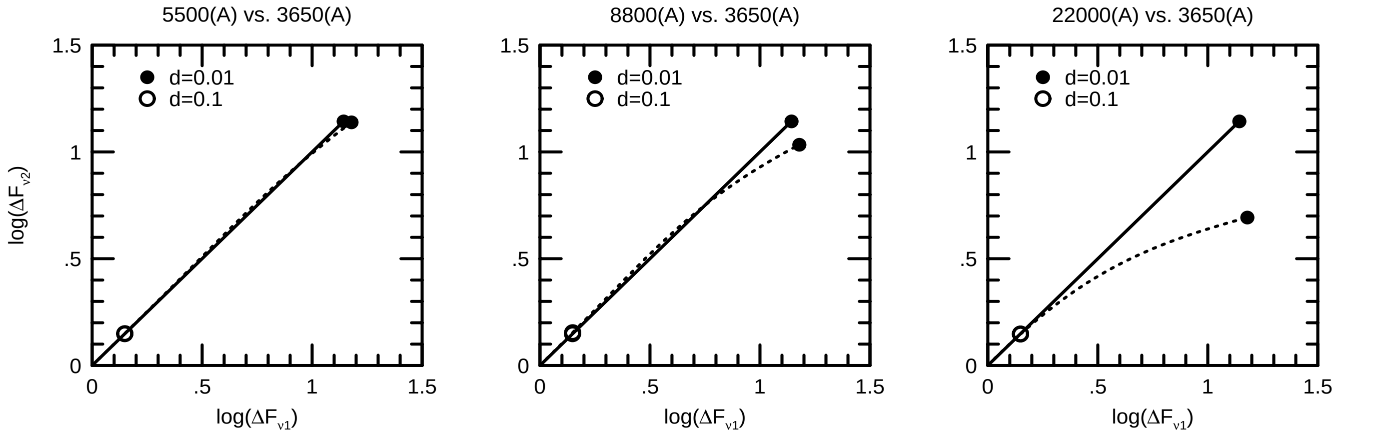

Fig. 10. The differences in the amplification factors at two different frequencies for the case of the standard disk (dotted line) and the optically thin flow (solid line). The adopted two frequencies are from the left, the U-band and the V-band (*left panels*), the U-band and the I-band (*middle panels*), and the U-band and the K-band (*right panels*). Open and filled circles represent the cases with $b = 0.1$ and $b = 0.01$, respectively. The lensing mass is assumed to be $M_{\rm lens} = 1.0 M_{\odot}$.

& Bahcall 1992). It is widely believed that microlensing does occur in Q 2237+0305 at a rate of at least one event per year, i.e. $\langle \Delta t \rangle \sim 1{\rm yr}$ (Corrigan et al. 1991; Houde & Racine 1994). Hence, the type of microlensing event which we would like to observe is expected to occur only once per 10 yr (for $b = 0.1$) to 100 yr (for $b = 0.01$).

We have demonstrated that an optically thick accretion disk exhibits more distinct features in its spectral shape than an optically thin accretion disk. Differences between these two disk models are, essentially, caused by different energy balance equations. In an optically thick accretion disk, generally, viscosity is small, accreting gas stays in the accretion disk for a much longer time than the disk rotation periods, so that the gravitational potential energy of the accreting gas can be effectively transformed into radiation on its way to the central compact object (in the present case, a supermassive black hole). In an optically thin accretion disk, on the other hand, since viscosity is high, accreting gas falls into the central compact object rapidly on a timescale of order the rotation period, and gravitational potential energy of accreting gas is not so effectively transformed into radiation (e.g., Kato, Fukue, & Mineshige 1998). Thus, most of gravitational potential energy of accreting gas is advected into the central compact object and is not radiated away. These major discriminant physical processes in the accretion disks can be distinguished by the microlens diagnostic technique.

In this paper, we assume that accretion disks are face-on to the observer. In a real situation, however, accretion disks will generally have non-zero inclination angles (i.e., $i \neq 0$). It will be complicated to quantitatively treat the dependence of inclination angles because of the increase in the number of parameters, such as the angle between the path of the lens object and the apparent semi-major axis caused by a non-zero inclination. Qualitatively, non-zero inclination affects the timescale of the microlensing event in such a way as to reduce the apparent disk size by a factor $\sim \cos i$. This effect seems to be small compared to others of interest unless the disk is nearly edge-on (i.e., $i \sim 90°$). This inclination effect will be systematically examined in future work.

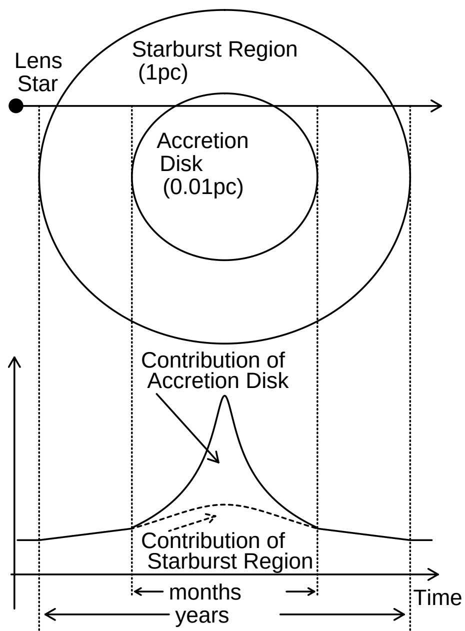

Fig. 11. A schematic view of a microlensing event of an AGN disk and circumnuclear starburst regions. The *upper* figure shows the situation for microlensing of an accretion disk plus its circumnuclear starburst region. The *lower* figure shows its expected light curve.

Finally, recent high-resolution observations, including those from *HST*, have revealed circumnuclear starburst regions in AGNs (see Umemura, Fukue, & Mineshige 1997, and references therein). If starburst regions exist around an accretion disk, microlensing of the AGN will produce a distinctive light curve; large-amplitude, short timescale variation (on a few month timescale) caused by the microlensing of the accretion disk will be superimposed on more gradual light variation (on a timescale of years) caused by the microlensing of the starburst region (see Fig. 11). (1992)). Thus, the contributions of these two components to the microlensing light curve will be easily separated. Long-term monitoring may provide a possible tool to elucidate the extension of circumnuclear starbursts although the presence of intrinsic variability tends to make such analyses complex.

5. Summary

The single-lens model adopted in this paper is a good approximation, unless the apparent separations among lens stars are of order the radius of the Einstein ring. But, as we noted above, the images of Q2237+0305 are generally subject to microlensing by multiple stars of the foreground galaxy. That is, we must next consider the microlensing events caused by the optical caustic pattern produced by multiple microlensing. Such events may occur more frequently with shorter durations and steeper magnification (Wambsganss & Kundić 1995). Light curves generated by caustic crossings may show even more interesting features than the present case (e.g., Schneider & Weiss 1986). A more realistic, analytically-approximated 'caustic' calculation has already been carried out for the case of Q 2237+0305 (Yonehara et al. 1998).

This diagnostic method for the central structure of AGN can be applied to other sources (e.g., MG0414+0534, PG1115+080, and the so-called 'clover leaf', H1413+117) of course.

Acknowledgements. We thank Joachim Wambsganß for valuable input. We also acknowledge the referee for his/her helpful comments. One of the authors (A.Y.) also thanks Hideyuki Kamaya for his encouragement. This work was supported in part by Research Fellowships of the Japan Society for the Promotion of Science for Young Scientists, 9852 (A.Y.), by the Japan-US Cooperative Research Program which is founded by the Japan Society for the Promotion of Science and the US National Science Foundation, and by the Grants-in Aid of the Ministry of Education, Science, Sports and Culture of Japan, 08640329 & 10640228 (S.M.).

References

Abramowicz M.A., Chen X., Kato S., Lasota J.-P., Regev O., 1995, ApJ 438, L37
Alcock C., et al., 1998, ApJ 499, L9
Blandford R.D., Hogg D.W., 1995, In: Kochanek C.S., Hewitt J.N. (eds.) IAU Symp. 173, Astrophysical Applications of Gravitational Lensing. Kluwer, Dordrecht, 355
Bontz R.J., 1979, ApJ 233, 402
Bromley B.C., 1996, ApJ 467, 537
Chang K., Refsdal S., 1984, A&A 132, 168
Corrigan R.T., et al., 1991, AJ 102, 34
Grieger B., Kayser R., Refsdal S., 1988, A&A 194, 54
Grieger B., Kayser R., Schramm T., 1991, A&A 252, 508
Houde M., Racine R., 1994, AJ 107, 466
Huchra J., Gorenstein M., Horine E., et al., 1985, AJ 90, 691
Irwin M.J., Webster R.L., Hewett P.C., Corrigan R.T., Jedrzejewski R.I., 1989, AJ 98, 1989
Jaroszyński M., Wambsganss J., Paczyński B., 1992, ApJ 396, L65
Kato, S., Fukue J., Mineshige S., 1998, Black-hole accretion disks. Kyoto University Press, Kyoto
Kundić T., et al., 1997, ApJ 482, 75
Manmoto T., Mineshige S., Kusunose M., 1997, ApJ 489, 791
Narayan R., Bartelmann M., 1996, astro-ph/9606001
Narayan R., Yi I., 1995, ApJ 452, 710
Paczyński B., 1986, ApJ 304, 1
Padmanabhan T., 1993, Structure formation in the universe. Cambridge University Press, New York
Rauch K.P., Blandford R.D., 1991, ApJ 381, L39
Rix H.-W., Schneider D.P., Bahcall J.N., 1992, AJ 104, 959
Rybicki G.B., Lightman A.P., 1979, Radiative Processes in Astrophysics. Wiley, New York
Schneider P., Weiss A., 1986, A&A 164, 237
Shakura N.I., Sunyaev R.A., 1973, A&A 24, 337
Umemura M, Fukue J., Mineshige S., 1997, ApJ 479, L97
Wambsganss J., Kundić T., 1995, ApJ 450, 19
Wambsganss J., Paczyński B., 1991, AJ 102, 864
Wambsganss J., Pazcyński B., Schneider P., 1990, ApJ 358, L33
Yonehara A., Mineshige S., Manmoto T., et al., 1998, ApJ 501, L41
Zheng W., Kriss G.A., Telfer R.C., Grimes J.P., Davidsen A.F., 1997, ApJ 475, 469